The Astrophysical Journal, 994:14 (11pp), 2025 November 20 https://doi.org/10.3847/1538-4357/ae102f
© 2025. The Author(s). Published by the American Astronomical Society.
OPEN ACCESS

The Prevalence of Bursty Star Formation in Low-mass Galaxies at $z = 1$–7 from Hα-to-UV Diagnostics

Marissa N. Perry[1], Anthony J. Taylor[1], Óscar A. Chávez Ortiz[1], Steven L. Finkelstein[1], Gene C. K. Leung[2], Micaela B. Bagley[1,3], Vital Fernández[4], Pablo Arrabal Haro[3], Katherine Chworowsky[1], Nikko J. Cleri[5,6,7], Mark Dickinson[8], Richard S. Ellis[9], Jeyhan S. Kartaltepe[10], Anton M. Koekemoer[11], Fabio Pacucci[12,13], Casey Papovich[14], Nor Pirzkal[15], and Sandro Tacchella[16,17]

[1] Department of Astronomy, The University of Texas at Austin, 2515 Speedway, Stop C1400, Austin, TX 78712, USA
[2] MIT Kavli Institute for Astrophysics and Space Research, 77 Massachusetts Ave., Cambridge, MA 02139, USA
[3] Astrophysics Science Division, NASA Goddard Space Flight Center, 8800 Greenbelt Rd, Greenbelt, MD 20771, USA
[4] Michigan Institute for Data Science, University of Michigan, 500 Church Street, Ann Arbor, MI 48109, USA
[5] Department of Astronomy and Astrophysics, The Pennsylvania State University, University Park, PA 16802, USA
[6] Institute for Computational and Data Sciences, The Pennsylvania State University, University Park, PA 16802, USA
[7] Institute for Gravitation and the Cosmos, The Pennsylvania State University, University Park, PA 16802, USA
[8] NSF's National Optical-Infrared Astronomy Research Laboratory, 950 N. Cherry Ave., Tucson, AZ 85719, USA
[9] Department of Physics & Astronomy, University College London, Gower Street, London, WC1E 6BT, UK
[10] Laboratory for Multiwavelength Astrophysics, School of Physics and Astronomy, Rochester Institute of Technology, 84 Lomb Memorial Drive, Rochester, NY 14623, USA
[11] Space Telescope Science Institute, 3700 San Martin Drive, Baltimore, MD 21218, USA
[12] Center for Astrophysics—Harvard & Smithsonian, 60 Garden St, Cambridge, MA 02138, USA
[13] Black Hole Initiative, Harvard University, 20 Garden St, Cambridge, MA 02138, USA
[14] George P. and Cynthia Woods Mitchell Institute for Fundamental Physics and Astronomy, Department of Physics and Astronomy, Texas A&M University, College Station, TX 77843-0001, USA
[15] ESA/AURA Space Telescope Science Institute, Baltimore, MD, USA
[16] Kavli Institute for Cosmology, University of Cambridge, Madingley Road, Cambridge, CB3 0HA, UK
[17] Cavendish Laboratory, University of Cambridge, 19 JJ Thomson Avenue, Cambridge, CB3 0HE, UK
Received 2025 August 2; revised 2025 September 30; accepted 2025 October 5; published 2025 November 11

Abstract

We present an analysis of the bursty star formation histories (SFHs) of 346 star-forming galaxies at $1 \lesssim z < 7$, selected from JWST/NIRSpec G395M and PRISM spectroscopy provided by the Cosmic Evolution Early Release Science (or CEERS) and Red Unknowns: Bright Infrared Extragalactic Survey (or RUBIES) surveys. We analyze the correlation of star formation rate versus stellar mass (the star-forming main sequence, SFMS) for our sample and find no significant difference between the intrinsic scatter in the Hα-based SFMS and the UV-continuum-based SFMS. However, the diagnostic power of the SFMS is limited at high redshift and low stellar mass due to observational biases that exclude faint, quenched galaxies. To more directly probe star formation variability, we examine the dust-corrected Hα-to-UV ratio, which is assumed to trace deviations from a constant SFH over the past $\sim$100 Myr. In our sample, 73^{+4}_{-4}% of galaxies exhibit Hα-to-UV ratios inconsistent with a constant SFH. We do not observe any statistically significant evolution in the Hα-to-UV ratio with redshift. Additionally, lower-mass galaxies ($7 \leqslant \log(M_*/M_\odot) < 8.5$) are 30% $\pm$ 1% more likely to lie above this equilibrium range—indicative of a recent ($\lesssim$100 Myr) burst of star formation—compared to higher-mass systems ($8.5 \leqslant \log(M_*/M_\odot) \leqslant 10.9$). These results suggest that bursty SFHs are more common in low-mass galaxies at $z \sim$ 1–7, and that this remains relatively stable across $\sim$0.8–6 Gyr after the Big Bang.

Unified Astronomy Thesaurus concepts: Early universe (435); Galaxy formation (595); Galaxy evolution (594); High-redshift galaxies (734)

1. Introduction

One of the most fundamental properties of a galaxy is the rate at which it forms stars—its star formation rate (SFR). At any given redshift, most galaxies follow a linear relationship between log SFR versus log stellar mass ($M_\star$), known as the star-forming main sequence (SFMS; E. Daddi et al. 2007; D. Elbaz et al. 2007; K. G. Noeske et al. 2007). Systems that lie above the intrinsic scatter of this relation are classified as "starburst" galaxies, while those that lie below are classified as "quiescent" galaxies. These classifications reflect an increased or decreased SFR relative to the typical value at a given stellar mass. A tight SFMS implies that galaxies of similar mass have similarly smooth and steady star formation histories (SFHs) over cosmic time, while increased scatter suggests more stochastic or bursty SFHs (e.g., K. G. Noeske et al. 2007; P. F. Hopkins et al. 2014; S. Shen et al. 2014; Y. Guo et al. 2016; R. Asquith et al. 2018; A. L. Faisst et al. 2019; S. Tacchella et al. 2020; H. Atek et al. 2022).

Observations increasingly support that star formation varies over cosmic time. In particular, galaxies at earlier epochs ($z \gtrsim 9$) exhibit more stochastic star formation than their later-time counterparts (e.g., L. Ciesla et al. 2024; J. W. Cole et al. 2025). Simulations predict that this transition arises from the gradual deepening of galaxy gravitational potentials over time, which increasingly stabilize gas outflows against internal

Original content from this work may be used under the terms of the Creative Commons Attribution 4.0 licence. Any further distribution of this work must maintain attribution to the author(s) and the title of the work, journal citation and DOI.

feedback mechanisms (e.g., P. Dayal et al. 2013; T. Kimm & R. Cen 2014; S. Tacchella et al. 2016; P. F. Hopkins et al. 2023; S. M. Wilkins et al. 2023). With JWST (J. P. Gardner et al. 2006, 2023), such stochasticity has been proposed as one of the possible key mechanisms behind the overabundance of UV-bright galaxies observed at $z \gtrsim 10$ (e.g., C. A. Mason et al. 2023; J. Mirocha & S. R. Furlanetto 2023; X. Shen et al. 2023; G. Sun et al. 2023a, 2023b; A. Kravtsov & V. Belokurov 2024; C. Carvajal-Bohorquez et al. 2025; R. S. Somerville et al. 2025). Indeed, the excess number density of bright galaxies observed by JWST, and its apparent lack of evolution between $z \sim 9$ and $z \sim 14$, already challenges standard model predictions (e.g., C. Conselice et al. 2023; S. L. Finkelstein et al. 2023, 2024; Y. Harikane et al. 2023; C. T. Donnan et al. 2024; L. Whitler et al. 2025), motivating a closer look at the physical mechanisms behind early star formation. Thus, characterizing the burstiness of early galaxies through their SFHs is essential for understanding the extent to which stochastic star formation contributes to the observed overabundance of UV-bright galaxies.

One approach to probing burstiness is to compare time-sensitive tracers of star formation. Two widely used tracers are nonresonant hydrogen recombination lines (e.g., Hα, Hβ) and the UV continuum. The luminosity of Balmer lines such as Hα (e.g., $L_{\rm H\alpha}$) originates from ionizing photons produced by massive, short-lived O stars and traces star formation over $\sim$10 Myr timescales. A galaxy's UV-continuum luminosity ($L_{\rm UV}$) is emitted by O stars as well as longer-lived B stars, and is traditionally assumed to trace star formation averaged over $\sim$100 Myr. However, both indicators are susceptible to several systematic effects. The Hα luminosity depends on the retention of Lyman continuum (LyC) photons, which can vary with galaxy stellar mass, redshift, and environment due to factors such as LyC escape and dust absorption (e.g., S. Tacchella et al. 2022b). Meanwhile, UV-based SFRs may be inflated by residual emission from older stellar populations, imposing a luminosity "floor" that can obscure recent variability—particularly in galaxies with declining or bursty SFHs (e.g., W. McClymont et al. 2025b). Recent modeling using Monte Carlo radiative transfer of nonionizing photons suggests that Hα and UV tracers are sensitive to shorter timescales than previously assumed, with Hα tracing $\sim$7–9 Myr and the UV continuum tracing $\sim$22–31 Myr (W. McClymont et al. 2025b). Moreover, both tracers require dust attenuation corrections, and the adoption of a single dust attenuation curve (i.e., D. Calzetti 2001) introduces additional uncertainty (e.g., Y. Guo et al. 2012; A. Broussard et al. 2019; A. Broussard et al. 2022; N. J. Cleri et al. 2022).

Despite these caveats, comparing $L_{\rm H\alpha}$ and $L_{\rm UV}$ provides a powerful diagnostic of recent star formation variability. During an episode of steady star formation, $L_{\rm H\alpha}$ reaches an equilibrium value much more quickly than $L_{\rm UV}$. Therefore, comparing both tracers allows us to detect recent variations in SFR over timescales of 10 Myr $\lesssim t \lesssim$ 100 Myr. Specifically, the logarithmic ratio $\log(L_{\rm H\alpha}/L_{\rm UV})$ (hereafter the Hα-to-UV ratio) can be used to determine if the SFR of a given galaxy has changed significantly over the past $\sim$100 Myr (e.g., K. Glazebrook et al. 1999; M. Sullivan et al. 2000, 2001; A. Broussard et al. 2019; N. Emami et al. 2019; A. L. Faisst et al. 2019; H. Atek et al. 2022; A. Broussard et al. 2022; Y. Asada et al. 2024; L. Clarke et al. 2024; R. Endsley et al. 2025).

The goal of this work is to use multiple SFR indicators to characterize the burstiness of star formation as a function of both redshift and stellar mass. We do this with a statistically robust sample of 346 star-forming galaxies, uniquely spanning a wide redshift range ($0.8 \leqslant z < 7$) and stellar mass range ($7.0 \leqslant \log(M_*/M_\odot) \leqslant 10.9$), exceeding the scope of many prior observational studies due to the ability of JWST to probe Hα to higher redshifts ($z \lesssim 7$) than possible from the ground.

We organize this work as follows. In Section 2, we describe the JWST/NIRSpec and JWST/NIRCam data used in our analysis. In Section 3, we outline methods used to derive the SFR indicators and galaxy stellar mass measurements. In Section 4 we present the derived galaxy properties, and in Section 5 we compare them to recent observations and simulations, discussing the implications of our results. Finally, we summarize our work in Section 6. Throughout this work, we use "ln" to represent the natural logarithm and "log" to represent the base-10 logarithm. We also assume a G. Chabrier (2003) initial mass function (IMF) and adopt a flat ΛCDM cosmology with parameters from Planck Collaboration et al. (2020): $\Omega_m = 0.315$ and $H_0 = 67.4\,{\rm km\,s^{-1}\,Mpc^{-1}}$.

2. Data

2.1. Spectroscopy

We use JWST/NIRSpec data from the Cosmic Evolution Early Release Science (CEERS) program (JWST ERS#1345, PI: Finkelstein; S. L. Finkelstein et al. 2017, 2024) and the Red Unknowns: Bright Infrared Extragalactic Survey (RUBIES) program (JWST Cycle 2 GO#4233, PIs: de Graaff and Brammer; A. G. de Graaff et al. 2023; B. Wang et al. 2024; A. de Graaff et al. 2025).

CEERS observed six NIRSpec/PRISM Micro-Shutter Array (MSA) pointings in the Extended Groth Strip (EGS) field, each for an effective integration time of 3107 s in the PRISM, G140M, G235M, and G395M dispersers. We use the internal CEERS collaboration v0.9 NIRSpec reduction (an evolution of the process detailed in P. Arrabal Haro et al. 2023a, 2023b). The full details of these reductions will appear in P. Arrabal-Haro et al. (2025, in preparation) and are summarized below.

The NIRSpec data were reduced using the JWST Calibration Pipeline v1.8.5 (H. Bushouse et al. 2022) and CRDS context `jwst_1029.pmap`. The data were reduced using the CRDS-prescribed pipeline parameters, with a few exceptions to improve the rejection of cosmic rays and "snowball" artifacts and to better optimize the width of the spectral apertures used to extract 1D spectra from the 2D spectra.

RUBIES observed six MSA pointings in the EGS field and 12 pointings in the Ultra Deep Survey (UDS) field, each for an effective exposure time of 2889 s in both the PRISM and G395M dispersers. In this work, we use the reduction of this data set first presented in A. J. Taylor et al. (2025). Briefly, A. J. Taylor et al. (2025) adopted the same JWST Calibration Pipeline modifications used in the CEERS v0.9 reductions (see above), but used a newer pipeline version (v1.13.4) and CRDS context (`1215.pmap`).

While this combined spectroscopic sample enables analysis of galaxies with a broad range of properties, it is subject to selection biases. Neither CEERS nor RUBIES implements a simple target selection function. CEERS targets are likely somewhat biased to bluer galaxies, as many were selected

from preexisting Hubble Space Telescope (HST)-based photometry before JWST imaging became available. RUBIES prioritized redder, brighter, JWST-selected sources. We examine the burstiness parameter used in our analysis—the Hα-to-UV ratio—and find that its distribution does not significantly differ between the CEERS and RUBIES targets. This suggests that, despite differing selection strategies, the two surveys probe galaxies with comparable levels of recent star formation variability.

2.2. Photometry

We use JWST/NIRCam imaging from the CEERS/EGS and PRIMER/UDS surveys. For CEERS, we use the v1.0 reductions described in M. B. Bagley et al. (2023) and in the Appendix of S. L. Finkelstein et al. (2025). For PRIMER (PI: Dunlop), we use an internal reduction from the PRIMER team (internal version 0.6). The PRIMER imaging data were reduced using the PRIMER Enhanced NIRCam Image Processing Library (or PENCIL; D. Magee et al. 2025, in preparation; J. Dunlop et al. 2025, in preparation) software. Both data sets include imaging in seven NIRCam broad bands (F090W, F115W, F150W, F200W, F277W, F356W, and F444W) and one medium band (F410M). Both data sets also include HST Advanced Camera for Surveys (ACS) optical imaging in F606W and F814W and Wide Field Camera 3 (WFC3) IR imaging in F105W (partial coverage), F125W, F140W, and F160W from the Cosmic Assembly Near-infrared Deep Extragalactic Legacy Survey (CANDELS; N. A. Grogin et al. 2011; A. M. Koekemoer et al. 2011), and partial coverage in F435W from UVCANDELS (V. Mehta et al. 2024). Our photometric catalog follows the procedure outlined in S. L. Finkelstein et al. (2024), with modest updates as described in several papers (e.g., V. Kokorev et al. 2025; A. J. Taylor et al. 2025). It is based on a combined F277W +F356W detection image, inclusive of point-spread function matching to ensure accurate colors across a wide wavelength baseline. Typical flux limits are listed in Tables 1 and 2 of S. L. Finkelstein et al. (2024).

3. Methods

3.1. Emission-line Fitting

We obtain spectroscopic redshift and emission-line information for 234 CEERS sources from an internal CEERS team spectroscopic redshift compilation, predominantly based on strong emission lines. The emission-line redshifts are measured using a Gaussian flux-weighted average of the centroids of the Gaussian profiles, based on the corresponding vacuum transition wavelengths from P. A. M. van Hoof (2018). These measurements were performed using LIME (see V. Fernández et al. 2024), with a visual inspection of the quality of the profile fittings. The line measurements from the CEERS sample are available online.[18]

We obtain spectroscopic redshifts for JWST/RUBIES sources using two methods. First, we collect spectroscopic redshifts available from the DAWN JWST Archive.[19] We additionally supplement these redshifts with a bespoke emission-line detection code. Briefly, this code searches for strong emission lines in NIRSpec spectra, and fits spectroscopic redshifts by comparing the velocity separations of detected lines to a list of strong emission lines typically observed in galaxies. This code is still a prototype, thus we visually inspect all spectroscopic redshifts estimated using this routine. In total, we compile 866 spectroscopic redshifts for RUBIES.

We identify and remove 62 galaxies likely dominated by active galactic nuclei (AGN) using the sample of AGN-dominated sources from CEERS and RUBIES identified in A. J. Taylor et al. (2025), which are selected based on the presence of broad Balmer emission lines. Additionally, we exclude sources at $z \geqslant 7$ from the sample, due to the Hα emission-line detection limit with JWST/NIRSpec.

Spectral resolution varies depending on redshift, with G395M grating or PRISM spectra selected to optimize Hα and Hβ line detection. For sources at $4.9 \leqslant z < 6.9$, we use G395M grating spectra to measure both Hα and Hβ for dust correction via the Balmer decrement and to derive dust-corrected Hα fluxes. For sources at $z < 3.4$ and $z \geqslant 6.9$, we use PRISM spectra for both purposes. For intermediate redshifts ($3.4 \leqslant z < 4.9$), we use PRISM spectra to measure the Balmer decrement and G395M spectra to derive dust-corrected Hα fluxes.

For sources observed with NIRSpec G395M grating spectra, we model the blended [N II]+Hα complex using a triple-Gaussian profile and a linear continuum, allowing us to isolate the Hα component by subtracting the [N II] contribution. The Hβ emission line is modeled with a single Gaussian and a linear continuum. For sources observed with PRISM spectra, we model Hα with a single Gaussian and a linear continuum due to the limited spectral resolution, and fit the blended Hβ +[O III] complex using a triple Gaussian and a linear continuum, subtracting the [O III] component to recover Hβ. Since we are unable to resolve the [N II] doublet with PRISM data, we correct the measured Hα+[N II] flux by applying a scaling factor of 0.98 ± 0.02, derived from the median Hα/([N II]+Hα) ratio measured in our sample of G395M sources, thereby estimating a deblended Hα flux for PRISM sources.

We perform initial fits of the emission lines using the CURVE_FIT function from `SciPy` (P. Virtanen et al. 2020) and pass these best-fit parameters as the starting points (with some perturbation to establish independent walkers) for the Markov Chain Monte Carlo (MCMC) fitting using the `emcee` package for Python (D. Foreman-Mackey et al. 2013). We use 32 walkers and a maximum of 3000 steps to sample the likelihood function and reach convergence, always discarding the first 2000 burn-in samples before evaluating the best-fit parameters.

We impose uniform priors on all model parameters: (1) emission-line amplitudes are constrained to be positive and less than twice the best-fit value returned by CURVE_FIT, in order to guide convergence while still allowing flexibility in the MCMC optimization, (2) line centers are allowed to vary within ±20 Å of the expected central wavelength, and (3) Gaussian widths are limited to the range 1.5–30 Å for the G395M grating and 30–200 Å for the PRISM data. These limits reflect the instrumental resolution floor of each mode, account for moderate emission-line blending, and accommodate typical galaxy velocity dispersions up to a few hundred kilometers per second. Lastly, (4) linear continua are required to be positive. For blended line complexes, we also enforce fixed [N II] and [O III] doublet ratios of 2.94:1 and 2.98:1,

[18] https://ceers-data.streamlit.app
[19] https://s3.amazonaws.com/msaexp-nirspec/extractions/nirspec_graded_v3.html

respectively, between the redder and bluer components. For each parameter, we report the median value of the MCMC sample distribution and we calculate the 1σ confidence interval by reporting the 16th and 84th percentile values. Calculating the area under each Gaussian fit, we obtain flux measurements of the emission lines present in each galaxy.

Through visual inspection of the line fits, we find and remove five broad-line AGN. We restrict our sample to galaxies with a signal-to-noise ratio (S/N) $\geqslant$3 for both the Hα and Hβ emission lines, such that we can compute a robust dust correction via the Balmer decrement. This results in 91/234 CEERS and 257/866 RUBIES star-forming galaxies with strong Hα and Hβ emission-line detections. Of these 348 sources, the Balmer decrement and Hα emission was measured with the G395M grating and PRISM for 133 and 94 sources, respectively. For the remaining 121 sources, the Balmer decrement was measured with PRISM and Hα emission was measured with the G395M grating.

We assume a D. Calzetti (2001) dust law to correct for nebular attenuation, with $E(B-V)$ values derived from the Balmer decrement. We adopt an intrinsic ratio of 2.87 for Hα/Hβ, corresponding to Case B recombination at an electron temperature T_e = 10,000 K and electron density $n_e = 10^2$ cm^{-3} (D. E. Osterbrock 1989). Finally, we convert the dust-corrected emission-line fluxes to luminosities using the spectroscopic redshift of each galaxy.

While the Case B recombination assumption is commonly used, we note that it may not hold for all galaxies—particularly in extreme ionization or density conditions—which can introduce deviations from the assumed intrinsic ratio and yield unphysical reddening values (i.e., $E(B-V) < 0$; e.g., W. McClymont et al. 2025a). We find 119/348 galaxies in our sample exhibit such negative values (ranging $-0.9 \leqslant E(B-V) < 0$), and we enforce $E(B-V) = 0$ for these cases to ensure physically meaningful results. The resulting distribution of extinction values spans $A_V = 0.0$–5.3 mag, with a median of $A_V = 0.5^{+1.2}_{-0.5}$ mag. We acknowledge that this nonnegligible population of sources with forced-zero reddening may impact the scatter in derived quantities that depend on dust correction, such as the Hα-to-UV ratio. Additionally, we emphasize that the true attenuation law may vary among galaxies and depend on galaxy properties such as dust geometry and optical depth (e.g., S. Tacchella et al. 2022a, 2022b; N. A. Reddy et al. 2025).

3.2. Spectral Energy Distribution Fitting

In this section, we outline how we fit the spectral energy distribution (SED) of each galaxy using the full suite of available photometry from JWST/NIRCam, HST/WFC3, and HST/ACS, spanning the rest-frame UV to IR. We cross-match the spectroscopic sample with the PRIMER/UDS, and CEERS/EGS and CANDELS/EGS photometric catalogs. We require the photometric and spectroscopic source positions to be separated by $<0\farcs3$. Some sources in the EGS field do not have NIRCam coverage; for those we use HST photometry from CANDELS.

We perform stellar population modeling with the SED-fitting code `BAGPIPES` (A. C. Carnall et al. 2018; A. C. Carnall et al. 2019) to measure the stellar masses and UV-continuum magnitude ($M_{1500\text{Å}}$) from the posterior spectra. We adopt a nonparametric SFH with the "bursty continuity" prior from S. Tacchella et al. (2023; see also J. Leja et al. 2019, for more discussion regarding burstiness priors). Our SFH model used logarithmically spaced time bins defined in look-back time.

The Universe's age at the redshift of interest is converted to megayears (Myr), and SFH bins are defined from 10 Myr up to just before the cosmic age using 10 logarithmic intervals (i.e., [10, 50, 100, ..., $t_{\text{universe}}(z)$]). An initial bin edge at 0 Myr is added at the beginning of the bin edge to ensure the full lookback time is covered.

We apply the Calzetti dust attenuation law (D. Calzetti et al. 2000), allowing the A_V parameter to vary between 0 and 3mag. Nebular emission is included, with the ionization parameter ($\log U$) allowed to vary between -4 and -1.

For the SFH, we specify the total mass formed, metallicity, and fractional deviations in SFR (Δ log SFR) in each time bin. We allow:

1. the total stellar mass formed to range between 10^{-4} and 10^{13} $M_\odot$; and
2. the metallicity to range between 0.01 and 5 $Z_\odot$, using a logarithmic prior (i.e., $\log_{10}$ prior).

Each SFH bin's star formation deviation parameter is assigned a Student's t-distribution prior with a prior scale of 2.0 to allow for bursty behavior, whenever present. These priors allow the model to flexibly fit a wide range of galaxy SFHs, including strongly burst-dominated scenarios.

The observed SED is interpolated to obtain the monochromatic flux density at 1500 Å in the rest frame ($F_{\nu,1500}$), which is then converted to an absolute AB magnitude at 1500 Å(M_{UV}).

To characterize the stellar masses of our NIRSpec sample, we compare them to those of a large (N = 101, 355) CEERS photometric sample derived with the `Dense Basis` SED-fitting code (K. Iyer & E. Gawiser 2017; K. G. Iyer et al. 2019), as described in K. Chworowsky et al. (2024). For each NIRSpec galaxy at spectroscopic redshift z_i, we identify a subsample ($N = 3000$) of CEERS galaxies with photometric redshifts closest to z_i and compute the CEERS conditional stellar mass percentiles at that redshift (16th–84th and 5th–95th). We find that 67.9% of our NIRSpec galaxies fall within the middle 68% of CEERS stellar masses at a matched redshift, and 93.2% fall within the middle 90%. These coverages are consistent with the nominal values expected for a random subsample, indicating that our NIRSpec sample fairly traces the CEERS stellar mass–redshift distribution.

3.3. UV-continuum Measurement

We convert the UV-continuum absolute magnitudes (M_{UV}) into luminosities (L_{UV}). To dust-correct these measurements, we apply the $E(B-V)$ values derived from the Balmer decrement, as described in Section 3.1. To account for the differential attenuation between nebular emission lines and stellar continuum light, we scale the nebular $E(B-V)$ values by a factor of 0.44 (D. Calzetti et al. 2000). We require a S/N $\geqslant$ 3 for the dust-corrected UV luminosities, which reduces the sample size by two galaxies.

The final combined CEERS and RUBIES sample includes 346 galaxies at $0.8 \leqslant z < 7$, with stellar masses spanning $7.0 \leqslant \log(M_*/M_\odot) \leqslant 10.9$. We summarize the physical quantities measured and derived above in Table 1 and show the spectroscopic redshift distribution of this sample in Figure 1. We separate the sample into redshift bins of $z = 1$–2.5, $z = 2.5$–4, $z = 4$–5.5, and $z = 5.5$–7 to track changes in galaxy

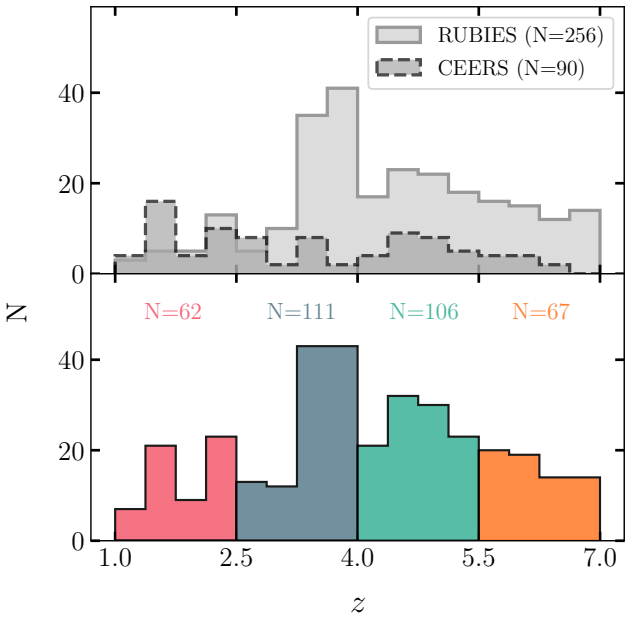


Figure 1. Spectroscopic redshift distribution of our sample split by survey (top) and by redshift bin (bottom). The full sample consists of 346 spectroscopically confirmed galaxies. We divide the sample into four redshift bins: $z = 1$–2.5, $z = 2.5$–4, $z = 4$–5.5, and $z = 5.5$–7, which we use throughout our analysis to examine redshift evolution in galaxy properties across cosmic time.

properties with cosmic time. These boundaries were chosen to ensure a minimum of ∼60 galaxies per bin, enabling statistically robust population-level analyses while also aligning with key epochs in cosmic SFH.

3.4. Stellar-mass Completeness

Before characterizing the SFMS, we construct a stellar-mass-complete sample. We estimate stellar mass completeness in each redshift bin following the method described in Section 5.2 of L. Pozzetti et al. (2010). For each galaxy, we compute the limiting stellar mass ($M_{\rm lim}$) it would have if its apparent magnitude (m_i) were equal to the limiting magnitude of the survey ($m_{\rm lim}$), assuming the galaxy has the same mass-to-light ratio. We define $m_{\rm lim}$ using the NIRCam F277W/F356W bands, where the median catalog 5σ depth is $m_{\rm lim} = 28.5$ (S. L. Finkelstein et al. 2025). These filters represent the continuum sensitivity that drives our stellar mass selection. For each galaxy with stellar mass $M_{*,i}$, the limiting stellar mass is given by

$$\log(M_{{\rm lim},i}) = \log(M_{*,i}) + 0.4\,(m_i - m_{\rm lim}) \quad . \tag{1}$$

In each redshift bin, we evaluate $M_{\rm lim,i}$ for the faintest 30% of galaxies and take the 90th percentile as the mass-completeness threshold. Our mass-completeness limits are shown in Table 2. Galaxies below these thresholds are excluded from subsequent SFMS fitting.

4. Results

4.1. The Star-forming Main Sequence

We calculate dust-corrected Hα- and UV-continuum-based SFRs using the calibrations from R. C. Kennicutt (1998), and apply a −0.24 dex correction to convert from a E. E. Salpeter (1955) to a G. Chabrier (2003) IMF.

Table 1
Summary of Derived Quantities

Quantity	Method
Redshift (z)	Spectroscopic line identification
Stellar mass (M_*)	SED fitting with `BAGPIPES`
Dust extinction (A_V)	Spectral line fitting of Hα/Hβ Balmer decrement
Hα luminosity ($L_{\rm H\alpha}$)	Spectral line fitting of Hα, dust-corrected using A_V values
UV luminosity ($L_{\rm UV}$)	SED fitting with `BAGPIPES`, dust-corrected using A_V values

Table 2
Stellar-mass-complete Sample Parameters

Redshift Bin	N	$\log(M_{\rm lim}/M_\odot)$	$\log(M_{\rm piv}/M_\odot)$
$1 \lesssim z \leqslant 2.5$	37	8.4	9.0
$2.5 < z \leqslant 4$	88	8.2	9.1
$4 < z \leqslant 5.5$	42	8.7	9.3
$5.5 < z < 7$	19	8.7	9.5

Note. For each redshift bin, $M_{\rm lim}$ is the limiting stellar mass computed in Section 3.4 and $M_{\rm piv}$ is the median stellar mass used for SFMS fitting in Section 4.1.

We model the relationship between SFR and stellar mass (M_*) using a linear relation of the form

$$y = m \times (\log M_* - \log M_{\rm piv}) + b, \tag{2}$$

where $y = \log(\mathrm{SFR}/M_\odot\ \mathrm{yr}^{-1})$, m is the slope, and b is the normalization at the pivot mass $M_{\rm piv}$. We define $M_{\rm piv}$ for each redshift bin in Table 2 as the median stellar mass. This reduces covariance between the slope and intercept during fitting.

To model observed scatter around the relation, we assume each observed data point $y_{{\rm obs},i}$ is drawn from a Gaussian distribution centered on the model prediction $y_{{\rm model},i}$ with total variance

$$y_{{\rm obs},i} \sim \mathcal{N}(y_{{\rm model},i},\ \sigma_i^2), \tag{3}$$

$$\sigma_i^2 = \sigma_{{\rm obs},i}^2 + \sigma_{\rm int}^2, \tag{4}$$

where $\sigma_{{\rm obs},i}$ is the 1σ measurement uncertainty on the $\log(\mathrm{SFR})$ of the ith data point, computed by propagating the SFR measurement error into log space, and $\sigma_{\rm int}$ represents the contribution of intrinsic scatter in the SFMS relation to the spread in $\log(\mathrm{SFR})$.

To account for sensitivity limits that impact the detectability of galaxies with faint star formation activity, we estimate limiting SFR values separately for Hα and UV-continuum observations. For our Hα-based measurements, this limit is set by the sensitivity of the NIRSpec G395M grating, with a 5σ detection threshold of 1.1×10^{-18} erg s^{-1} cm^{-2} (S. L. Finkelstein et al. 2025). Although some Hα-based SFRs were measured with PRISM, the higher spectral resolution of G395M defines an upper limit on our detection capabilities for this sample. For the UV-continuum-based measurements, we estimate a 3σ limiting SFR(UV) using the posterior distributions of rest-frame UV-continuum magnitudes ($M_{\rm UV}$) from our SED-fitting (Section 3.2). For each redshift bin, we adopt the maximum of the 16th percentile $M_{\rm UV}$ values across the sample, representing the faintest reliably measured UV-continuum level consistent with the photometry.

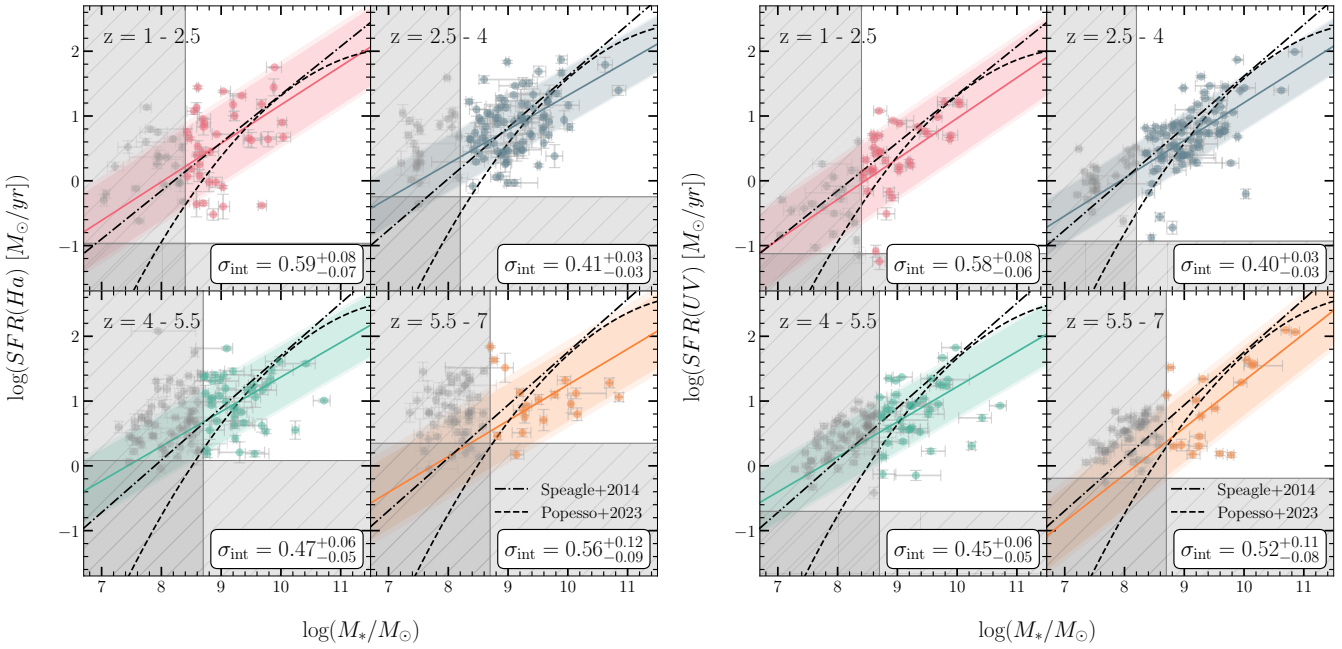


Figure 2. Hα-based (left) and UV-continuum-based (right) SFRs vs. stellar masses for our galaxy sample binned by redshift. Vertical gray regions and gray data points indicate where our sample is not mass complete, as defined in Section 3.4. These data points are excluded from the fitting procedure. In the left panel, horizontal gray regions indicate the 5σ NIRSpec G395M grating emission-line sensitivity limits derived from Table 6 in S. L. Finkelstein et al. (2025). In the right panel, we compute 3σ limiting SFR(UV) values based on the faintest reliably measured rest-frame UV-continuum in each redshift bin, defined as the maximum of the 16th percentile $M_{1500\text{Å}}$ values from our SED-fitting posteriors of galaxies with S/N > 3. The colored shaded regions denote the 1$\sigma_{\rm int}$ intrinsic scatter intervals about the SFMS and its associated error. The black dashed and dashed–dotted curves represent literature values from P. Popesso et al. (2023) and J. S. Speagle et al. (2014), respectively. On average, the Hα-based SFMS and the UV-based SFMS exhibit the same degree of intrinsic scatter, indicating that we do not detect short-timescale (∼10 Myr) SFR variability across the sample with the SFMS.

To model completeness effects near these limits, we incorporate a sigmoid-based selection function $\Phi(y)$:

$$\Phi(y) = \frac{1}{1 + \exp[-\alpha \times (y - \log_{10}(\mathrm{SFR}_{\rm lim}))]}, \quad (5)$$

where $\mathrm{SFR}_{\rm lim}$ is the limiting SFR and α controls the sharpness of the transition from incomplete to complete. We fix $\alpha = 5$ for all redshift bins, corresponding to a moderate transition in completeness over a range of ∼0.3 dex. This formulation allows the model to reduce the weight of galaxies near the sensitivity threshold without discarding them, mitigating bias in the slope and scatter estimates.

We model the log-likelihood function for our fit as

$$\ln \mathcal{L}(\theta) = -\frac{1}{2}\sum_i \left[\frac{(y_{\mathrm{obs},i} - y_{\mathrm{model},i})^2}{\sigma_i^2} + \ln(\sigma_i^2) \right] + \sum_i \ln \Phi(y_{\mathrm{obs},i}), \quad (6)$$

where $\theta = \{m, b, \sigma_{\rm int}\}$ are the model parameters.

We estimate the posterior distributions of the parameters using an MCMC sampler with 20 walkers and 5000 total steps, discarding the first 3000 steps as burn-in. We adopt uniform priors: $m \in [0.5, 1.5]$, $b \in [-5, 5]$, and $\sigma_{\rm int} \in [0, 1.5]$, consistent with constraints from prior studies (e.g., J. S. Speagle et al. 2014; K. E. Whitaker et al. 2014; B. Salmon et al. 2015; P. Popesso et al. 2023). We report the median and 16th–84th percentile values from the posterior distributions. We plot the Hα- and UV-continuum-based SFRs versus stellar masses in Figure 2 and provide our best-fit results in Table 3. Horizontal gray regions indicate areas where we do not expect to detect galaxies due to survey sensitivity limits. The regime where our sample is mass incomplete, as defined in Section 3.4, is indicated by the vertical gray regions and gray data points.

We compute the intrinsic scatter—averaged across the probed redshift range—for both SFMS relations to be $\langle\sigma_{\rm H\alpha}\rangle = 0.45 \pm 0.03$ dex and $\langle\sigma_{\rm UV}\rangle = 0.44 \pm 0.02$ dex. The difference, $\langle\sigma_{\rm H\alpha}\rangle - \langle\sigma_{\rm UV}\rangle = 0.01 \pm 0.04$ dex, is consistent with zero and therefore not statistically significant for our sample.

The mass-incomplete subsamples exhibit visually flatter Hα-based SFMS relations compared to the best-fit relations given by the mass-complete subsample and relations reported by P. Popesso et al. (2023) and J. S. Speagle et al. (2014), especially at high redshifts ($z \gtrsim 5.5$). This deviation likely arises from two factors: (1) sensitivity limits in the NIRSpec observations that bias against low-SFR galaxies, artificially elevating the observed SFMS, and (2) increased star formation variability in low-mass galaxies at early times, enhancing the number of galaxies observed during a burst phase (e.g., M. Sparre et al. 2017; D. Pelliccia et al. 2020; G. Sun et al. 2023a; Y. Asada et al. 2024; K. Daikuhara et al. 2024; V. Gelli et al. 2025; W. McClymont et al. 2025b). Together, these effects limit the SFMS's ability to recover the full distribution of star formation states, and may obscure burst-driven variability in the Hα scatter.

4.2. The Hα-to-UV Luminosity Ratio

To more directly probe burstiness in galaxy SFHs, we turn to an independent diagnostic: the Hα-to-UV luminosity ratio. In our analysis, we use attenuation-corrected luminosities for both Hα and UV. This ratio is sensitive to recent changes in

Table 3
Star-forming Main Sequence Best-fit Parameters

SFR Indicator	Redshift Bin	m	b	$\sigma_{\rm int}$
Hα	$1 \lesssim z \leqslant 2.5$	$0.59^{+0.12}_{-0.07}$	$0.58^{+0.10}_{-0.09}$	$0.59^{+0.08}_{-0.07}$
Hα	$2.5 < z \leqslant 4$	$0.53^{+0.04}_{-0.02}$	$0.85^{+0.05}_{-0.05}$	$0.41^{+0.03}_{-0.03}$
Hα	$4 < z \leqslant 5.5$	$0.53^{+0.06}_{-0.03}$	$1.00^{+0.07}_{-0.07}$	$0.47^{+0.06}_{-0.05}$
Hα	$5.5 < z < 7$	$0.55^{+0.09}_{-0.04}$	$1.00^{+0.13}_{-0.13}$	$0.56^{+0.12}_{-0.09}$
UV	$1 \lesssim z \leqslant 2.5$	$0.63^{+0.15}_{-0.09}$	$0.34^{+0.10}_{-0.10}$	$0.58^{+0.08}_{-0.06}$
UV	$2.5 < z \leqslant 4$	$0.58^{+0.08}_{-0.05}$	$0.69^{+0.04}_{-0.04}$	$0.40^{+0.03}_{-0.03}$
UV	$4 < z \leqslant 5.5$	$0.54^{+0.06}_{-0.03}$	$0.84^{+0.07}_{-0.07}$	$0.45^{+0.06}_{-0.05}$
UV	$5.5 < z < 7$	$0.72^{+0.18}_{-0.14}$	$0.98^{+0.12}_{-0.12}$	$0.52^{+0.11}_{-0.08}$

Note. All parameters are computed from galaxy SFRs as a function of stellar mass. For each redshift bin, parameters are derived within the range over which we are stellar mass complete, as outlined in Table 2. Note that b is the normalization at the subsample median stellar mass ($M_{\rm piv}$).

SFR on timescales of ∼10–100 Myr and offers a complementary view to the SFMS-based analysis.

We explore how the Hα-to-UV luminosity ratio of galaxies in our sample changes with redshift and stellar mass. We compare these results to an equilibrium range of $\log(L_{\rm H\alpha}/L_{\rm UV}) = [-1.93, -1.78]$ as predicted by stellar population synthesis models assuming a constant SFH over the past ∼100 Myr and metallicities ($\log(Z/Z_\odot)$) between −2 and 0 (V. Mehta et al. 2023). This convention is widely adopted in the literature (e.g., K. Glazebrook et al. 1999; M. Sullivan et al. 2000, 2001; A. Broussard et al. 2019; N. Emami et al. 2019; A. L. Faisst et al. 2019; H. Atek et al. 2022; A. Broussard et al. 2022; Y. Asada et al. 2024; L. Clarke et al. 2024; R. Endsley et al. 2025) as it reflects the characteristic timescales traced by Hα and UV emission. Thus, the equilibrium range provides a consistent benchmark for identifying short-timescale burstiness independent of cosmic epoch. In Figure 3, we show the Hα-to-UV ratio distributions for each redshift bin. The distributions are approximately Gaussian and peak within the equilibrium range expected for a constant SFH over the past ∼100 Myr. However, the distribution at $z = 5.5$–7 exhibits a tail or possible bimodality toward lower Hα-to-UV ratio values. We interpret this feature as originating from high-mass ($9 \lesssim \log(M_*/M_\odot) \leqslant 10.9$) galaxies that fall below the Hα-based SFMS in Figure 2. This suggests a recent decline in star formation activity among massive galaxies at high redshift.

In Figure 4, we plot the Hα-to-UV ratio as a function of stellar mass and redshift. For each stellar mass bin, we quantify the scatter in the Hα-to-UV ratio using the standard deviation and estimate its uncertainty via bootstrap resampling. We find no significant difference in the average scatter between lower-mass ($7 \leqslant \log(M_*/M_\odot) < 8.5$) and higher-mass ($8.5 \leqslant \log(M_*/M_\odot) \leqslant 10.9$) galaxies in our sample, with $\langle\sigma_{\rm low\text{-}mass}\rangle - \langle\sigma_{\rm high\text{-}mass}\rangle = -0.04 \pm 0.04$ dex (left panel). However, across all redshifts lower-mass galaxies exhibit higher Hα-to-UV ratios, consistent with more burst-driven star formation (right panel).

5. Discussion

5.1. Fraction around the Hα-to-UV Equilibrium

To characterize these results further, we compute the fraction of galaxies in our sample that lie above ($f_{\rm above}$), below ($f_{\rm below}$), and within ($f_{\rm eq}$) the Hα-to-UV ratio equilibrium range calculated by V. Mehta et al. (2023), which corresponds to a constant SFH over the past ∼100 Myr. A galaxy is classified as within the equilibrium range if its 1σ uncertainty interval overlaps the range defined by V. Mehta et al. (2023).

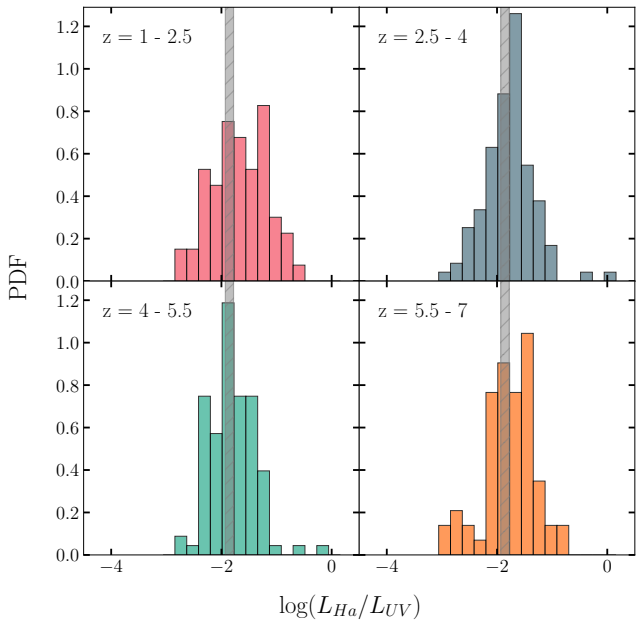


Figure 3. The distribution of Hα-to-UV ratio values binned by redshift. The vertical gray hatched region shows the equilibrium range of the Hα-to-UV ratio calculated by V. Mehta et al. (2023). For each redshift bin, the distribution peak lies within the equilibrium range expected for a constant SFH over the past ∼100 Myr.

We compute these fractions using a probabilistic approach that propagates individual measurement uncertainties into the population-level distribution. For each galaxy, we perturb the observed Hα-to-UV ratio by drawing from a Gaussian distribution centered on the measured value with a standard deviation set by its 1σ uncertainty. We then resample these perturbed values via bootstrap resampling and compute the fractions for each resample. The final estimates for $f_{\rm above}$, $f_{\rm below}$, and $f_{\rm eq}$ are taken as the median of the bootstrap distributions, and the uncertainties are defined by the 16th and 84th percentiles.

We find that 73^{+4}_{-4}% of galaxies in our sample have Hα-to-UV ratios that lie either above or below the equilibrium range defined by V. Mehta et al. (2023), and are therefore inconsistent with a constant SFH over the past ∼100 Myr. We find no variation in this statistic between our lower-mass and higher-mass samples. Furthermore, averaging across all redshifts, we find lower-mass galaxies exhibit a higher fraction above $f_{\rm above} = 0.53^{+0.05}_{-0.05}$ and a lower fraction below $f_{\rm below} = 0.18^{+0.04}_{-0.03}$ compared to higher-mass galaxies with $f_{\rm above} = 0.33^{+0.04}_{-0.04}$ and $f_{\rm below} = 0.41^{+0.04}_{-0.04}$.

For comparison, L. Clarke et al. (2024) report that 48%–71% of their spectroscopic sample of 146 galaxies from CEERS and JADES at $z \sim 1.4$–7 and with $7.0 \leqslant \log(M_*/M_\odot) \leqslant 10.5$ deviate from a constant SFH. Applying the same selection to our sample, we recover 73^{+4}_{-4}%, which is consistent within uncertainties. At $z \sim 4.7$–6.5 and with $6.0 \leqslant \log(M_*/M_\odot) \leqslant 10.5$, Y. Asada et al. (2024) find 60% of their photometric sample of 125 galaxies from CANUCS deviate from a constant SFH. For a

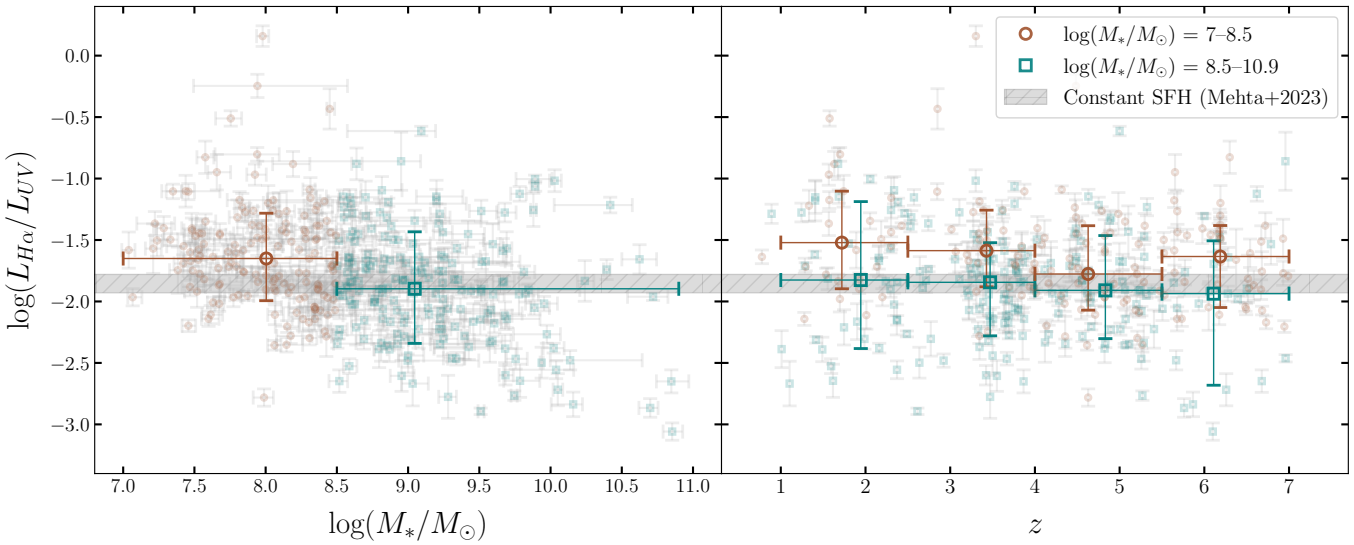


Figure 4. Left panel: the Hα-to-UV ratio vs. stellar mass for our galaxy sample binned by stellar mass. The large points represent the median values in each stellar mass bin. The vertical error bars denote the 16th and 84th percentiles of each bin and the horizontal error bars denote the stellar mass range of each bin. The horizontal gray hatched region shows the equilibrium range of the Hα-to-UV ratio calculated by V. Mehta et al. (2023). Right panel: the Hα-to-UV ratio vs. redshift for our galaxy sample binned by stellar mass. The large points represent the median values in each stellar mass and redshift bin. The vertical error bars denote the 16th and 84th percentiles of each bin and the horizontal error bars denote the redshift range of each bin. Lower-mass galaxies maintain higher Hα-to-UV ratio values across all redshifts probed compared to higher-mass galaxies, suggesting lower-mass galaxies are more prone to bursty star formation.

Table 4
Fraction of Galaxies around the Hα-to-UV Ratio Equilibrium Range

Redshift Bin	Mass Bin	$f_{\rm above}$	$f_{\rm eq}$	$f_{\rm below}$
$1 \lesssim z \leqslant 2.5$	$7 < \log(M_*/M\odot) < 8.5$	$0.67^{+0.13}_{-0.08}$	$0.21^{+0.13}_{-0.08}$	$0.08^{+0.08}_{-0.04}$
$1 \lesssim z \leqslant 2.5$	$8.5 < \log(M_*/M\odot) < 10.9$	$0.44^{+0.09}_{-0.09}$	$0.15^{+0.09}_{-0.06}$	$0.41^{+0.09}_{-0.09}$
$2.5 < z \leqslant 4$	$7 < \log(M_*/M\odot) < 8.5$	$0.61^{+0.09}_{-0.09}$	$0.27^{+0.09}_{-0.09}$	$0.12^{+0.06}_{-0.06}$
$2.5 < z \leqslant 4$	$8.5 < \log(M_*/M\odot) < 10.9$	$0.32^{+0.05}_{-0.06}$	$0.28^{+0.06}_{-0.05}$	$0.41^{+0.06}_{-0.06}$
$4 < z \leqslant 5.5$	$7 < \log(M_*/M\odot) < 8.5$	$0.41^{+0.08}_{-0.06}$	$0.33^{+0.08}_{-0.08}$	$0.27^{+0.06}_{-0.06}$
$4 < z \leqslant 5.5$	$8.5 < \log(M_*/M\odot) < 10.9$	$0.30^{+0.07}_{-0.06}$	$0.30^{+0.07}_{-0.07}$	$0.41^{+0.06}_{-0.07}$
$5.5 < z < 7$	$7 < \log(M_*/M\odot) < 8.5$	$0.53^{+0.06}_{-0.09}$	$0.28^{+0.09}_{-0.06}$	$0.19^{+0.06}_{-0.06}$
$5.5 < z < 7$	$8.5 < \log(M_*/M\odot) < 10.9$	$0.26^{+0.13}_{-0.09}$	$0.30^{+0.13}_{-0.13}$	$0.43^{+0.13}_{-0.09}$

matched subsample, we measure 72^{+4}_{-4}%, a modestly higher fraction that may reflect differences in sample selection and methodology (e.g., SED-derived galaxy properties from photometry and inclusion of gravitationally lensed systems).

In their analysis of 368 galaxies at $z \sim 6$ with $-22.0 \leqslant M_{\rm UV} \leqslant -15.8$, R. Endsley et al. (2025) found that high-redshift UV-faint galaxies may be more likely to be observed in recent downturns in their SFR, and therefore have Hα-to-UV ratios below the equilibrium range. These galaxies, which exhibit suppressed Hα emission relative to their UV continuum, are often referred to as "temporarily quiescent"—systems that have recently experienced a decline in SFR following a burst phase, but which may resume elevated star formation on short timescales. Similarly, the SERRA zoom-in simulations (V. Gelli et al. 2025) suggest that the fraction of temporarily quiescent galaxies at $6 < z < 8$ increases with decreasing mass (from $\lesssim$40% at $M_* > 10^8 M_\odot$ to $\gtrsim$60% at $M_* < 10^8 M_\odot$). Additional simulation-based work using IllustrisTNG and ASTRID indicates that lower-mass quenched galaxies tend to reside in denser environments than their star-forming counterparts (E. J. Weller et al. 2025), pointing to environment as a potential driver of quenching at high redshift.

In our sample, fractional measurements for galaxies with similar properties to these works (high redshift: $5.5 \leqslant z < 7$, low stellar mass: $7.0 \leqslant \log(M_*/M_\odot) < 8.5$, and faint: $-20.83 \leqslant M_{\rm UV} \leqslant -18.16$) are given in the second-to-last row in Table 4. We find a high fraction above the equilibrium range ($f_{\rm above} = 0.53^{+0.06}_{-0.09}$) and a low fraction below it ($f_{\rm below} = 0.19^{+0.06}_{-0.06}$), suggesting that a substantial portion of our lower-mass, UV-faint galaxies are observed during burst phases. These empirical results contrast with the trends inferred from some simulations and observational studies that predict a higher prevalence of temporarily quiescent systems in this regime.

5.2. The Duty Cycle of Star Formation

We also consider how the duty cycle of star formation—probed through these fractional values—evolves with redshift. L. Clarke et al. (2024) found their data reveal no consistent trend with redshift, but suggest a low duty cycle ($f_{\rm below} > f_{\rm above}$) between $z = 1.4$–4 and a high duty cycle ($f_{\rm above} > f_{\rm below}$) between $z = 4$–5. As seen in Figure 5, our results provide new insight into the galaxy populations driving these trends. We find that higher-mass galaxies maintain a low duty cycle across all redshifts probed except $1 \leqslant z < 2.5$, while lower-mass galaxies exhibit a high duty cycle at all redshifts. Our results are broadly consistent with recent observational

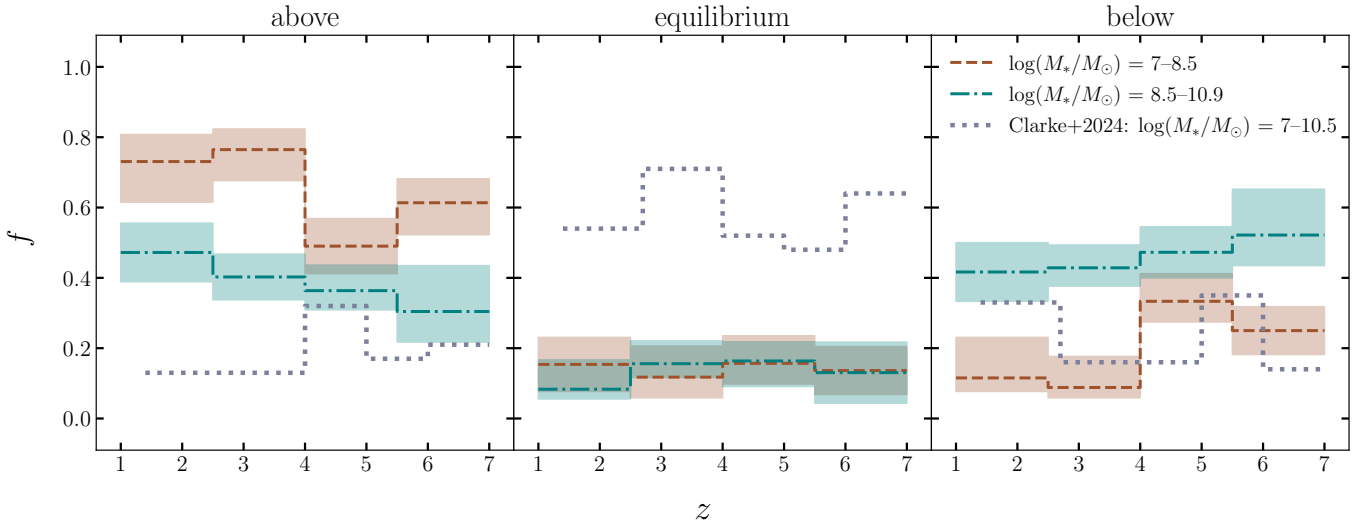


Figure 5. The fraction of galaxies whose Hα-to-UV ratios are consistent (middle panel) and inconsistent (outer panels) with a constant SFH computed by V. Mehta et al. (2023) shown as a function of redshift. For each stellar mass and redshift bin, we perturb the observed ratios using Gaussian noise based on 1σ errors and compute fractions via bootstrap resampling. Measured values correspond to the median of the bootstrap distribution, with error bars from the 16th and 84th percentiles. Colored curves represent this work, binned by stellar mass and redshift, compared to the dotted gray curve from L. Clarke et al. (2024), which includes galaxies with stellar masses in the range 10^7–$10^{10.5} M_*/M_\odot$. Within each bin, we compute the median redshift value. We estimate uncertainties on the fractions using bootstrap resampling. These trends suggest little evolution in the relative fraction of galaxies above, below, or within the equilibrium range over z = 1–7.

work using CEERS data. J. W. Cole et al. (2025) examined SFHs for galaxies at $4.5 < z \leqslant 9$ and found that, on average, lower-mass galaxies ($8.7 \leqslant \log(M_*/M_\odot) < 9.3$) exhibit SFHs that are approximately constant over 10–100 Myr timescales, whereas higher-mass galaxies ($9.3 \leqslant \log(M_*/M_\odot) \leqslant 10.3$) tend to show declining SFHs over the same periods. In their highest-redshift bins ($6 < z \leqslant 7$ and $7 < z \leqslant 9$), they report that the fraction of lower-mass galaxies with rising recent SFRs ($\log(\mathrm{SFR}_{10}/\mathrm{SFR}_{100}) > 0$) exceeds 50%, consistent with burst-dominated SFHs in this regime.

Furthermore, we compute the redshift-binned difference in the fractional values between z = 1–2.5 and z = 5.5–7, as summarized in Table 5. These results indicate that there is no evolution in the duty cycle across $1 \lesssim z < 7$. These findings suggest that the relative balance between bursty and steady star formation remains roughly constant over z = 1–7.

5.3. Limitations and Sources of Bias

To contextualize these findings, we next consider how selection effects may influence our measurements, particularly for low-mass galaxies at high redshift. Galaxies experiencing a burst of star formation are bright and easy to detect, whereas galaxies in quiescent or postburst phases are difficult to observe, especially at high redshift. Even after a recent burst, the most massive stars in a galaxy die off within ∼10 Myr, causing both the nebular emission lines and the UV continuum to fade rapidly. This effect is more pronounced for low- to moderate-mass galaxies at high redshift. Using the high-redshift suite (X. Ma et al. 2018a, 2018b) of the second-generation Feedback in Realistic Environments (FIRE-2; P. F. Hopkins et al. 2018) cosmological zoom-in simulations, G. Sun et al. (2023a) estimated only 50% of moderate-mass ($M_*/M_\odot \sim 10^{8.5}$–$10^9$) galaxies at $z \sim 7$ can be detected by surveys such as JADES and CEERS, and that galaxies near this detection limit tend to have experienced a recent burst of star formation. As a result, our lower-mass ($7 \leqslant \log(M_*/M_\odot) < 8.5$), high-redshift ($z$ = 5.5–7) sample is likely biased toward galaxies experiencing bursts within the past ∼10 Myr or galaxies undergoing frequent, short-timescale bursts every ∼100 Myr (V. Mehta et al. 2023). For CEERS galaxies, this bias is exacerbated by the NIRSpec slit selection, which for $z < 7$ galaxies predominantly targets UV-bright sources. Together, these selection effects may artificially inflate the observed burstiness of low-mass, high-redshift galaxies by underrepresenting quiescent or postburst systems. Consequently, the true fraction of galaxies with steady or recently declining SFHs is likely higher than observed, and our measured values of f_{above} and σ_{int} may be skewed toward more extreme, burst-dominated populations. These trends should be interpreted with caution, as it may lead to overestimating the presence of bursty star formation in the early Universe.

Furthermore, while our analysis removes broad-line AGN, we do not explicitly exclude narrow-line AGN from the sample. Narrow-line AGN, which may not significantly contribute to the rest-frame UV emission due to the obscuration and orientation of these systems, could nonetheless enhance nebular line emission such as Hα, potentially mimicking elevated SFRs. Although the impact is likely limited, especially given the rarity of luminous AGN at these masses and redshifts, the potential contamination by narrow-line AGN should be considered when interpreting the results of this work.

Finally, we note that several key modeling assumptions may introduce systematic uncertainties that could influence our results. These include (1) adopting a single attenuation law

Table 5
Fractional Shift in Galaxies around the Hα-to-UV Ratio Equilibrium Range between $1 \lesssim z \leqslant 2.5$ and $5.5 < z < 7$

Stellar Mass	$\Delta f_{\mathrm{above}}$	Δf_{eq}	$\Delta f_{\mathrm{below}}$
$7 < \log(M_*/M\odot) < 8.5$	$-0.13^{+0.15}_{-0.10}$	$0.07^{+0.14}_{-0.12}$	$0.11^{+0.10}_{-0.08}$
$8.5 \leqslant \log(M_*/M\odot) < 10.9$	$-0.18^{+0.12}_{-0.16}$	$0.15^{+0.16}_{-0.14}$	$0.02^{+0.16}_{-0.12}$

Note. We define Δf as the difference in the fraction of galaxies above, below, and within the Hα-to-UV equilibrium range between the z = 5.5–7 and z = 1–2.5 bins. Quoted uncertainties are propagated from the measurement errors in each bin.

(i.e., D. Calzetti 2001) for all galaxies, (2) assuming Case B recombination with fixed nebular conditions, and (3) applying a constant ratio between nebular and continuum attenuation across the full redshift and stellar mass range. While these assumptions are motivated by a desire for consistency with previous literature, the magnitude of their potential impact may be comparable to the differences we observe in Hα-to-UV ratios and SFMS scatter across redshift and stellar mass. In particular, recent works indicate that the attenuation-curve slope evolves with redshift, becoming steeper at $z \lesssim 3$ and flatter at $z \gtrsim 5$ (e.g., V. Markov et al. 2025; I. Shivaei et al. 2025). While we do not observe a redshift evolution over $z = 1$–7 in galaxy burstiness (as probed by the Hα-to-UV ratio), adopting a redshift-dependent attenuation law (i.e., Equations (5) and (6) from I. Shivaei et al. 2025) could introduce one. A steeper curve at low redshift would lower the Hα-to-UV ratio, suppressing the inferred burstiness, whereas a flatter curve at high redshift would raise the Hα-to-UV ratio, increasing the inferred burstiness. Future work should aim to quantify the sensitivity of burstiness indicators to these assumptions.

6. Summary

In this work, we analyze the SFMS and the Hα-to-UV ratio of a statistically robust sample of 346 star-forming galaxies at $1 \lesssim z < 7$ in the CEERS and RUBIES spectroscopic surveys to investigate the burstiness of star formation at these redshifts. Our main conclusions are as follows:

1. We find that the difference in intrinsic scatter between the Hα-based SFMS and UV-continuum-based SFMS, $\langle\sigma_{\mathrm{H}\alpha}\rangle - \langle\sigma_{\mathrm{UV}}\rangle = 0.01 \pm 0.04$ dex, is consistent with zero and therefore not statistically significant for our stellar-mass-complete subsample.
2. The mass-incomplete subsample exhibits visually flatter Hα-based SFMS relations compared to the best-fit relations given by the mass-complete subsample and literature relations, especially at high redshifts ($z \gtrsim 5.5$). This may be due to a combination of (1) NIRSpec sensitivity limits that bias against low-SFR galaxies—artificially raising the average observed SFR—and (2) elevated Hα emission from galaxies undergoing bursts of star formation. These effects limit the utility of the SFMS in identifying individual bursty galaxies and motivate a complementary diagnostic approach.
3. To more directly probe recent ($\lesssim$100 Myr) SFR variability, we examine the dust-corrected Hα-to-UV ratio. We find evidence for bursty star formation in 73^{+4}_{-4}% of galaxies in our sample based on their Hα-to-UV ratios, calculated as the combined fraction of sources above and below the equilibrium range defined by V. Mehta et al. (2023). We find no variation in this total bursty fraction between our lower-mass and higher-mass subsamples. However, the distribution of bursty systems differs with mass: A higher fraction of lower-mass galaxies lie above the equilibrium range ($f_{\mathrm{above}} = 0.53^{+0.05}_{-0.05}$) and a lower fraction below it ($f_{\mathrm{below}} = 0.18^{+0.04}_{-0.03}$) compared to higher-mass galaxies with $f_{\mathrm{above}} = 0.33^{+0.04}_{-0.04}$ and $f_{\mathrm{below}} = 0.41^{+0.04}_{-0.04}$. Thus, we find lower-mass galaxies are 30% $\pm$ 1% more likely to be observed in a recent ($\lesssim$100 Myr) burst of star formation compared to their higher-mass counterparts.
4. We infer the evolutionary pathway of galaxies around the Hα-to-UV equilibrium range by computing the fractional change Δf in Hα-to-UV ratios between $z = 1$–2.5 and $z = 5.5$–7. Across both mass bins, we find that Δf values are statistically consistent with zero, suggesting little to no evolution in the relative fraction of galaxies above, below, or within the equilibrium range over $z = 1$–7.

With the upcoming JWST surveys such as the CAPERS program (JWST Cycle 3 GO#6368, PI: Dickinson; M. Dickinson et al. 2024), future robust analyses breaking upward the redshift range of the current paper are possible with JWST, and would probe the SFH of the earliest galaxies in the Universe.

Acknowledgments

The authors would like to thank Bahram Mobasher, Benne Holwerda, Mauro Giavalisco, Michaela Hirschmann, and Stephen Wilkins for thorough and detailed feedback, which helped improve the quality of this manuscript. We thank the RUBIES team (including PIs Anna de Graaff and Gabriel Brammer) for carrying out this program and making the data publicly available. M.N.P. acknowledges support for the Galaxy Evolution Vertically Integrated Project (GEVIP) undergraduate research group from the National Science Foundation under NSF-AAG-1908817 and NSF-AAG-2009905.

The JWST data presented in this article were obtained from the Mikulski Archive for Space Telescopes (MAST) at the Space Telescope Science Institute. The specific observations analyzed can be accessed via DOI: 10.17909/0eta-ym85.

ORCID iDs

Marissa N. Perry https://orcid.org/0009-0008-1378-4381
Anthony J. Taylor https://orcid.org/0000-0003-1282-7454
Óscar A. Chávez Ortiz https://orcid.org/0000-0003-2332-5505
Steven L. Finkelstein https://orcid.org/0000-0001-8519-1130
Gene C. K. Leung https://orcid.org/0000-0002-9393-6507
Micaela B. Bagley https://orcid.org/0000-0002-9921-9218
Vital Fernández https://orcid.org/0000-0003-0531-5450
Pablo Arrabal Haro https://orcid.org/0000-0002-7959-8783
Katherine Chworowsky https://orcid.org/0000-0003-4922-0613
Nikko J. Cleri https://orcid.org/0000-0001-7151-009X
Mark Dickinson https://orcid.org/0000-0001-5414-5131
Richard S. Ellis https://orcid.org/0000-0001-7782-7071
Jeyhan S. Kartaltepe https://orcid.org/0000-0001-9187-3605
Anton M. Koekemoer https://orcid.org/0000-0002-6610-2048
Fabio Pacucci https://orcid.org/0000-0001-9879-7780
Casey Papovich https://orcid.org/0000-0001-7503-8482
Nor Pirzkal https://orcid.org/0000-0003-3382-5941
Sandro Tacchella https://orcid.org/0000-0002-8224-4505

References

Arrabal Haro, P., Dickinson, M., Finkelstein, S. L., et al. 2023a, ApJL, 951, L22
Arrabal Haro, P., Dickinson, M., Finkelstein, S. L., et al. 2023b, Natur, 622, 707
Asada, Y., Sawicki, M., Abraham, R., et al. 2024, MNRAS, 527, 11372
Asquith, R., Pearce, F. R., Almaini, O., et al. 2018, MNRAS, 480, 1197

Atek, H., Furtak, L. J., Oesch, P., et al. 2022, MNRAS, 511, 4464
Bagley, M. B., Finkelstein, S. L., Koekemoer, A. M., et al. 2023, ApJL, 946, L12
Broussard, A., Gawiser, E., & Iyer, K. 2022, ApJ, 939, 35
Broussard, A., Gawiser, E., Iyer, K., et al. 2019, ApJ, 873, 74
Bushouse, H., Eisenhamer, J., Dencheva, N., et al. 2022, JWST Calibration Pipeline, v1.8.5, Zenodo, doi:10.5281/zenodo.7429939
Calzetti, D. 2001, PASP, 113, 1449
Calzetti, D., Armus, L., Bohlin, R. C., et al. 2000, ApJ, 533, 682
Carnall, A. C., McLure, R. J., Dunlop, J. S., & Davé, R. 2018, MNRAS, 480, 4379
Carnall, A. C., McLure, R. J., Dunlop, J. S., et al. 2019, MNRAS, 490, 417
Carvajal-Bohorquez, C., Ciesla, L., Laporte, N., et al. 2025, arXiv:2507.13160
Chabrier, G. 2003, PASP, 115, 763
Chworowsky, K., Finkelstein, S. L., Boylan-Kolchin, M., et al. 2024, AJ, 168, 113
Ciesla, L., Elbaz, D., Ilbert, O., et al. 2024, A&A, 686, A128
Clarke, L., Shapley, A. E., Sanders, R. L., et al. 2024, ApJ, 977, 133
Cleri, N. J., Trump, J. R., Backhaus, B. E., et al. 2022, ApJ, 929, 3
Cole, J. W., Papovich, C., Finkelstein, S. L., et al. 2025, ApJ, 979, 193
Conselice, C., Adams, N., Austin, D., Trussler, J., & De Albernaz Ferreira, L. 2023, AAS Meeting, 241, 153.07
Daddi, E., Dickinson, M., Morrison, G., et al. 2007, ApJ, 670, 156
Daikuhara, K., Kodama, T., Pérez-Martínez, J. M., et al. 2024, MNRAS, 531, 2335
Dayal, P., Dunlop, J. S., Maio, U., & Ciardi, B. 2013, MNRAS, 434, 1486
de Graaff, A., Brammer, G., Weibel, A., et al. 2025, A&A, 697, A189
de Graaff, A. G., Brammer, G., Bezanson, R., et al. 2023, A Complete Census of the Rare, Extreme and Red: A NIRCam-selected Extragalactic Community Survey with JWST/NIRSpec, JWST Proposal. Cycle 2, ID. #4233,
Dickinson, M., Amorin, R., Arrabal Haro, P., et al. 2024, The CANDELS-Area Prism Epoch of Reionization Survey (CAPERS), JWST Proposal. Cycle 3, ID. #6368,
Donnan, C. T., McLure, R. J., Dunlop, J. S., et al. 2024, MNRAS, 533, 3222
Elbaz, D., Daddi, E., Le Borgne, D., et al. 2007, A&A, 468, 33
Emami, N., Siana, B., Weisz, D. R., et al. 2019, ApJ, 881, 71
Endsley, R., Chisholm, J., Stark, D. P., Topping, M. W., & Whitler, L. 2025, ApJ, 987, 189
Faisst, A. L., Capak, P. L., Emami, N., Tacchella, S., & Larson, K. L. 2019, ApJ, 884, 133
Fernández, V., Amorín, R., Firpo, V., & Morisset, C. 2024, A&A, 688, A69
Finkelstein, S. L., Bagley, M. B., Arrabal Haro, P., et al. 2025, ApJL, 983, L4
Finkelstein, S. L., Bagley, M. B., Ferguson, H. C., et al. 2023, ApJL, 946, L13
Finkelstein, S. L., Dickinson, M., Ferguson, H. C., et al. 2017, The Cosmic Evolution Early Release Science (CEERS) Survey, Early Release Science, JWST Proposal. Cycle 0, ID. #1345,
Finkelstein, S. L., Leung, G. C. K., Bagley, M. B., et al. 2024, ApJL, 969, L2
Foreman-Mackey, D., Hogg, D. W., Lang, D., & Goodman, J. 2013, PASP, 125, 306
Gardner, J. P., Mather, J. C., Abbott, R., et al. 2023, PASP, 135, 068001
Gardner, J. P., Mather, J. C., Clampin, M., et al. 2006, SSRv, 123, 485
Gelli, V., Pallottini, A., Salvadori, S., et al. 2025, ApJ, 985, 126
Glazebrook, K., Blake, C., Economou, F., Lilly, S., & Colless, M. 1999, MNRAS, 306, 843
Grogin, N. A., Kocevski, D. D., Faber, S. M., et al. 2011, ApJS, 197, 35
Guo, Y., Giavalisco, M., Cassata, P., et al. 2012, ApJ, 749, 149
Guo, Y., Rafelski, M., Faber, S. M., et al. 2016, ApJ, 833, 37
Harikane, Y., Ouchi, M., Oguri, M., et al. 2023, ApJS, 265, 5
Hopkins, P. F., Gurvich, A. B., Shen, X., et al. 2023, MNRAS, 525, 2241
Hopkins, P. F., Kereš, D., Oñorbe, J., et al. 2014, MNRAS, 445, 581
Hopkins, P. F., Wetzel, A., Kereš, D., et al. 2018, MNRAS, 480, 800
Iyer, K., & Gawiser, E. 2017, ApJ, 838, 127
Iyer, K. G., Gawiser, E., Faber, S. M., et al. 2019, ApJ, 879, 116
Kennicutt, R. C., Jr. 1998, ARA&A, 36, 189
Kimm, T., & Cen, R. 2014, ApJ, 788, 121
Koekemoer, A. M., Faber, S. M., Ferguson, H. C., et al. 2011, ApJS, 197, 36
Kokorev, V., Chávez Ortiz, Ó. A., Taylor, A. J., et al. 2025, ApJL, 988, L10
Kravtsov, A., & Belokurov, V. 2024, arXiv:2405.04578
Leja, J., Carnall, A. C., Johnson, B. D., Conroy, C., & Speagle, J. S. 2019, ApJ, 876, 3
Ma, X., Hopkins, P. F., Boylan-Kolchin, M., et al. 2018a, MNRAS, 477, 219
Ma, X., Hopkins, P. F., Garrison-Kimmel, S., et al. 2018b, MNRAS, 478, 1694
Markov, V., Gallerani, S., Ferrara, A., et al. 2025, NatAs, 9, 458
Mason, C. A., Trenti, M., & Treu, T. 2023, MNRAS, 521, 497
McClymont, W., Tacchella, S., D'Eugenio, F., et al. 2025a, MNRAS, 540, 190
McClymont, W., Tacchella, S., Smith, A., et al. 2025b, MNRAS, 544, 513
Mehta, V., Rafelski, M., Sunnquist, B., et al. 2024, ApJS, 275, 17
Mehta, V., Teplitz, H. I., Scarlata, C., et al. 2023, ApJ, 952, 133
Mirocha, J., & Furlanetto, S. R. 2023, MNRAS, 519, 843
Noeske, K. G., Weiner, B. J., Faber, S. M., et al. 2007, ApJL, 660, L43
Osterbrock, D. E. 1989, Astrophysics of Gaseous Nebulae and Active Galactic Nuclei (Melville, NY: University Science Books)
Pelliccia, D., Mobasher, B., Darvish, B., et al. 2020, ApJL, 896, L26
Planck Collaboration, Aghanim, N., Akrami, Y., et al. 2020, A&A, 641, A6
Popesso, P., Concas, A., Cresci, G., et al. 2023, MNRAS, 519, 1526
Pozzetti, L., Bolzonella, M., Zucca, E., et al. 2010, A&A, 523, A13
Reddy, N. A., Shapley, A. E., Sanders, R. L., et al. 2025, arXiv:2506.17396
Salmon, B., Papovich, C., Finkelstein, S. L., et al. 2015, ApJ, 799, 183
Salpeter, E. E. 1955, ApJ, 121, 161
Shen, S., Madau, P., Conroy, C., Governato, F., & Mayer, L. 2014, ApJ, 792, 99
Shen, X., Vogelsberger, M., Boylan-Kolchin, M., Tacchella, S., & Kannan, R. 2023, MNRAS, 525, 3254
Shivaei, I., Naidu, R. P., Rodríguez Montero, F., et al. 2025, arXiv:2509.01795
Somerville, R. S., Yung, L. Y. A., Lancaster, L., et al. 2025, MNRAS, in press
Sparre, M., Hayward, C. C., Feldmann, R., et al. 2017, MNRAS, 466, 88
Speagle, J. S., Steinhardt, C. L., Capak, P. L., & Silverman, J. D. 2014, ApJS, 214, 15
Sullivan, M., Mobasher, B., Chan, B., et al. 2001, ApJ, 558, 72
Sullivan, M., Treyer, M. A., Ellis, R. S., et al. 2000, MNRAS, 312, 442
Sun, G., Faucher-Giguère, C.-A., Hayward, C. C., & Shen, X. 2023a, MNRAS, 526, 2665
Sun, G., Faucher-Giguère, C.-A., Hayward, C. C., et al. 2023b, ApJL, 955, L35
Tacchella, S., Dekel, A., Carollo, C. M., et al. 2016, MNRAS, 457, 2790
Tacchella, S., Eisenstein, D. J., Hainline, K., et al. 2023, ApJ, 952, 74
Tacchella, S., Finkelstein, S. L., Bagley, M., et al. 2022a, ApJ, 927, 170
Tacchella, S., Forbes, J. C., & Caplar, N. 2020, MNRAS, 497, 698
Tacchella, S., Smith, A., Kannan, R., et al. 2022b, MNRAS, 513, 2904
Taylor, A. J., Finkelstein, S. L., Kocevski, D. D., et al. 2025, ApJ, 986, 165
van Hoof, P. A. M. 2018, Galax, 6, 63
Virtanen, P., Gommers, R., Oliphant, T. E., et al. 2020, NatMe, 17, 261
Wang, B., Leja, J., de Graaff, A., et al. 2024, ApJL, 969, L13
Weller, E. J., Pacucci, F., Ni, Y., Hernquist, L., & Park, M. 2025, ApJ, 979, 181
Whitaker, K. E., Franx, M., Leja, J., et al. 2014, ApJ, 795, 104
Whitler, L., Stark, D. P., Topping, M. W., et al. 2025, ApJ, 992, 63
Wilkins, S. M., Vijayan, A. P., Lovell, C. C., et al. 2023, MNRAS, 518, 3935